Driven responses of periodically patterned superconducting films

A. Al Luhaibi [1,2] A. Glatz [3,4] and J. B. Ketterson [1]

[1]*Department of Physics and Astronomy, Northwestern University, Evanston, Illinois 60208, USA*
[2]*Physics Department, King Fahd University of Petroleum and Minerals, 31261 Dhahran, Saudi Arabia*
[3]*Materials Science Division, Argonne National Laboratory, 9700 S. Cass Avenue, Argonne, Illinois 60439, USA*
[4]*Department of Physics, Northern Illinois University, DeKalb, Illinois 60115, USA*

(Received 5 August 2022; revised 3 December 2022; accepted 8 December 2022; published xxxxxxxxxx)

We simulate the motion of a commensurate vortex lattice in a periodic lattice of artificial circular pinning sites having different diameters, pinning strengths, and spacings using the time-dependent Ginzburg-Landau formalism. Above some critical DC current density J_c, the vortices depin, and the resulting steady-state motion then induces an oscillatory electric field $E(t)$ with a defect "hopping" frequency f_0, which depends on the applied current density and the pinning landscape characteristics. The frequency generated can be locked to an applied AC current density over some range of frequencies, which depends on the amplitude of the DC as well as the AC current densities. Both synchronous and asynchronous collective hopping behaviors are studied as a function of the supercell size of the simulated system and the (asymptotic) synchronization threshold current densities determined.

DOI: 10.1103/PhysRevB.00.004500

I. INTRODUCTION

Above some magnetic field H_{c1}, the field penetrates type-II superconductors as quantized vortices carrying a flux quantum, producing the so-called mixed state. An external current density, $\mathbf{J}$, subjects each vortex to a Lorentz force in the direction perpendicular to the current density and field, $\mathbf{F}_L = \mathbf{J} \times \mathbf{H}$. In the absence of some restraining (pinning) force, vortices move and dissipation associated with the finite conductivity of their moving normal cores results in a finite potential drop across the superconductor. However, structural and other irregularities result in finite pinning forces which in turn result in some critical depinning current density J_c for the onset of dissipation, above which a finite potential drop appears. (This current density is generally much smaller than the depairing current density required to break Cooper pairs). For two or more decades there has been much interest in incorporating artificial defects to increase pinning and with it J_c, particularly in films where there is more access to the sample interior to introduce the defects; examples include: patterned arrays of holes (anti dots) [1,2] or normal [3] or ferromagnetic metallic dots [4,5] as well alterations induced by particle beams as in heavy ion irradiation. When the applied current density, $|\mathbf{J}|$, exceeds the critical current density, vortices break loose from their pinning sites and move. In a spatially periodic system the resulting motion can generate temporally periodic pinning and depinning cycles with some current density-dependent frequency, here called the *hopping* frequency, see Sec. III. By introducing an additional AC current density into the system with a frequency approximating the unperturbed hopping frequency, the two can be locked within some finite, amplitude-dependent, bandwidth, Sec. IV. In what follows we will model this behavior by numerically solving the time-dependent Ginzburg-Landau equations (TDGL), which will be briefly reviewed in Sec. II A. Section II B explains the system that is simulated. While much of the research involving artificial pinning sites focuses on maximizing J_c [6–11], the results obtained here suggest that certain dynamic effects, and possible applications thereof, merit increased attention.

II. MODEL

The formulation of the TDGL equations utilized here follows that of Sadovskyy *et al.* [12] which allows the specification of defect positions, sizes and other characteristics, as explained in Sec. II A. The particular systems simulated here are described in Sec. II B.

A. Theory

The TDGL equations can be written in the following dimensionless form:

$$u(\partial_t + \imath\mu)\psi = \epsilon(\mathbf{r})\psi - |\psi|^2\psi + (\nabla - \imath\mathbf{A})^2\psi, \quad (1)$$

$$\kappa^2 \nabla \times (\nabla \times \mathbf{A}) = \mathbf{J}_s + \mathbf{J}_n, \quad (2)$$

Here ψ and $\mathbf{A}$ are the order parameter and the vector potential respectively, μ is the scalar potential, $\mathbf{J}_n$ and $\mathbf{J}_s$ are the normal and super current densities, and $\kappa = \lambda_0/\xi_0$ is the Ginzburg-Landau parameter. Here we consider thin films and therefore use the $\kappa \to \infty$ limit and the Landau gauge for $\mathbf{A}$. The unit of length is given by the zero-temperature coherence length, ξ_0, and the unit of time, $t_0 = \sigma m_e/(2e^2\psi_0^2)$, is determined by the typical relaxation time of the TDGL equation, $\tau_\psi = \Gamma/\nu_0$, and the relaxation time of the vector potential, $\tau_A \propto \sigma/\psi_0^2$; here ν_0 is the density of states at the Fermi level, σ the normal conductivity, $\Gamma = \frac{\nu_0 \pi \hbar}{8 k_B T_c}$ a relaxation parameter, T_c the critical

temperature, e and m_e the electron charge and mass, and ψ_0 the equilibrium value of the order parameter, where the latter is determined by the ratio of linear and nonlinear coefficients of the dimensionless TDGL equation, or alternatively the London penetration length $\lambda_0^2 = m_e c^2/(8\pi e^2 \psi_0^2)$. These also define the dimensionless relaxation parameter $u = \Gamma/(\nu_0 t_0)$, which we set to 1 in our simulations.

Here we model pinning by so-called δT_c pinning [13], where the critical temperature is spatially modulated. In Eq. (1), this is realized through the coefficient of the linear GL term, $\epsilon(\mathbf{r}) = T_c(\mathbf{r})/T - 1$. In the superconductor we use a value of $\epsilon = 1$ and within the pinning site $\epsilon < 1$, i.e., the local critical temperature of the pinning site is less than the bulk T_c. For values $0 < \epsilon < 1$ one has weakly superconducting defects whereas regions with $\epsilon < 0$ model normal defects.

The magnetic field and, correspondingly, the vector potential are measured in units of the upper critical field $H_{c2}(0) = \phi_0/(2\pi\xi_0^2)$ ($\phi_0 = \pi\hbar c/e$ is the flux quantum). The total current density can be written as

$$\mathbf{J} = \mathbf{J}_s + \mathbf{J}_n = \mathrm{Im}\,[\psi^*(\nabla - \imath\mathbf{A})\psi] - (\nabla\mu + \partial_t \mathbf{A}), \qquad (3)$$

where the unit of the current density is given by $J_0 = e\hbar/(m_e\xi_0)\psi_0^2$. In these units, the depairing current density has the value $J_{dp} = 2/\sqrt{27} \approx 0.385$. At applied current densities near the depairing current density above the free-flux flow regime, amplitude fluctuations of the superconducting order parameter become large such that above some current density $J \cong 0.3$ the local amplitude could become zero which can lead to the creation of fluctuating vortex/antivortex pairs in the system.

Here we apply an external current density in x direction of form

$$J_{ext,x}(t) = J_{dc} + J_{ac}\sin(2\pi f_{ext} t). \qquad (4)$$

Important to note is that the TDGL formalism is valid as long as equilibrium excitations are small and the system remains in a steady state. Therefore we only consider frequencies $f_{ext} \ll \tau_\psi^{-1}$. Furthermore, we ensure that the peak applied current density $J_{dc} + J_{ac}$ stays well below the depairing current density such that order parameter fluctuations can be neglected. For a more detailed discussion of nonequilibrium effects we refer to the book by Kopnin [14]. We will discuss typical material parameters for current and frequency as well as vortex velocities in the discussion section.

For the numerical solution of equations (1), the system is discretized on a regular two-dimensional mesh in space (with a typical grid spacing of $0.3\xi_0$) and the time integration is performed by using an implicit Crank-Nicolson scheme (typical time discretization $0.1t_0$). These discretized equations are then simulated on GPUs using an iterative Jacobi solver. We use periodic boundary conditions in both directions and the external current is applied in x direction which is realized by ensuring that it matches the average total current following Ref. [12].

B. Simulation

In most parts of this work, we are interested in the vortex dynamics of a superconducting film having a regular square lattice of (weakly superconducting) circular pinning centers, where the applied current direction is rotated 45° with respect to the principle axis of the square array. The reason for studying this rotated configuration is that enlarged systems show enhanced stability of the moving vortex lattice compared to a square pinning array.

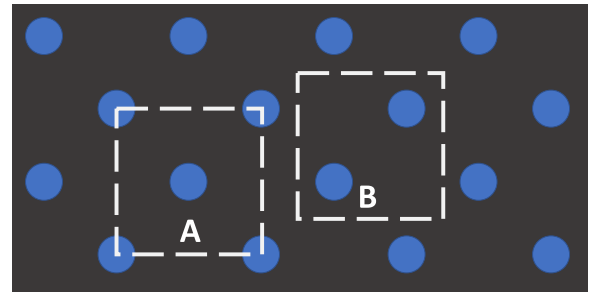

FIG. 1. (a) a simple square lattice drawn as centered square lattice with two pinning sites per square. (b) Moving the site centers along the square diagonal removes those at the corners.

The magnetic field is applied perpendicular (taken as the z direction) to the film with a strength corresponding to the first matching field (see also Ref. [15]), i.e., one vortex per pinning site. Therefore we restrict our simulations mostly to a single unit cell of the pinning array with periodic boundary conditions, which implies that the steady-state dynamics of all vortices in the extended system is synchronized. We will also discuss the collective stability in an enlarged unit cell, which we refer to as *supercell*, in Sec. V). This will remove the (artificial) synchronization enforced by periodic boundary conditions involving a single unit cell. Since we are interested in low-temperature applications of synchronized vortex dynamics, we neglect thermal fluctuations in the TDGL equations. We start our simulations for a simple unit cell of linear size $\sqrt{2}L$ having two offset circular pinning sites with diameter D with an in-plane DC current, J_{dc}, applied in x direction [see Fig. 1(b)]. Here L is the pinning array lattice constant or, in other words, the distance between two nearest neighbor pinning sites. Note that the two unit cells outlined in Figs. 1(a) and 1(b) are equivalent, but we choose (b) for better visualization purposes. Figure 2 shows the squared amplitude of the complex order parameter, $|\psi|^2$, as 3D surface plot and flat projection at the bottom at three different stages of a single oscillation of the electric field. A corresponding time-trace of the electric field with markers of panels (a)–(c) is shown in Fig. 3 and an animation is shown in supplemental movie 1 [16]. Panel (a) corresponds to the lowest dissipation state, where the vortex is inside the defect, panel (b) just between the pinning sites in a "free-flow" state with intermediate dissipation, and panel (c) just before getting trapped by a defect again. In the latter case, the vortices are pulled into the defect by the pinning force, which accelerates the vortices and therefore increases the dissipation to its maximum. Furthermore, this panel also illustrates the unit cell geometry in more detail (length $\sqrt{2}L$ with circular defect of diameter D and strength ϵ). Our benchmark system is defined by $L = 10$, $D = 5$, and $\epsilon = 0.75$, i.e., the pinning site is a weakly superconducting defect.

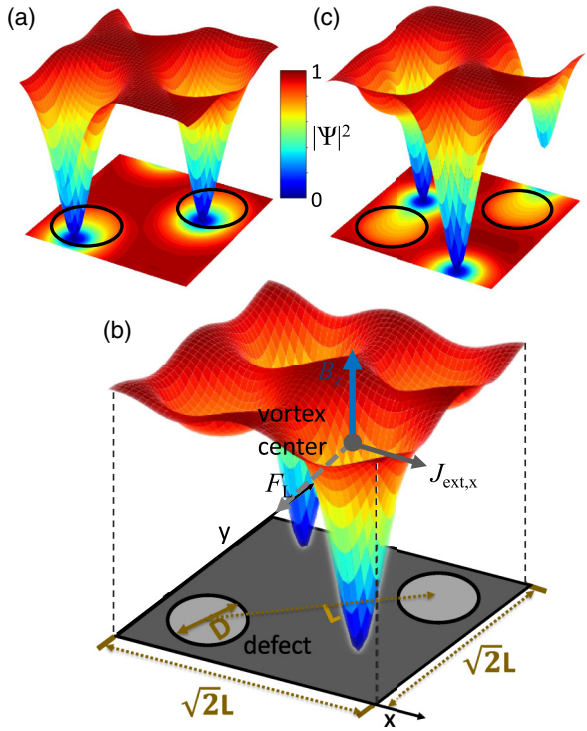

FIG. 2. Surface plots of $|\psi|^2$ in the simulated system of size $\sqrt{2}L \times \sqrt{2}L$ with two circular defects of diameter D (indicated by the circles) separated by L representing a unit cell of a large pinning array for different vortex positions in the system corresponding to different phases of a cycle (see also Fig. 3): (a) vortex is moving inside the defect, (b) vortex is the farthest from defects, and (c) vortex is about to enter the defect. The projection at the bottom of (b) indicates regions with different T_c/ϵ values in dark gray ($\epsilon = 1$) and light gray ($\epsilon = 0.75$). At the center position of the vortex, the direction of applied current, magnetic field, and resulting Lorentz force (F_L) are indicated.

III. RESPONSE TO A CONSTANT (DC) CURRENT DENSITY

We begin our study of the unit cell dynamics by determining the current density-electric field (J-E) behavior for systems with differing unit cell sizes, $2L^2$, and defects. As it is well known, vortices depin and start moving if the applied DC current density exceeds the critical value J_c in the direction perpendicular to the applied current and field (here the y direction). Since we are studying the regime $J_{dc} > J_c$, vortices show alternating pinning and depinning motion between second nearest neighbor sites which are separated by the unit cell size $\sqrt{2}L$.

Figure 4 shows some J-E characteristics for various values of L, D, and ϵ. Note that the electric field is averaged over at least 10 complete oscillation periods of $E(t)$, i.e., we plot $\langle E \rangle (J_{dc})$. As expected, the critical current density J_c decreases with ϵ for fixed L and D. Note that in our simulations, no additional pinning due to bulk disorder or edges is considered—see Sec. VI.

Increasing the diameter D from 5 to 7.5 does not change the critical current density significantly. However, the dependence of the critical current density on the defect diameter and area fraction, $\nu = \pi D^2/(4L^2)$, which defects occupy in the simulated region, is typically monotonic and has a maximum for a fixed ν and D. A detailed analysis can be found in Refs. [8,9]. The size of a pinning site defines its curvature (since we are studying circular defects), which has an optimal value for largest pinning force. For $L = 10$ and $D = 5$, the area fraction is close to 20%, which is close to the optimal area fraction for largest possible critical current density. Note that in our case the values of ϵ are positive and therefore still allow for weak superconductivity inside the defects. This influences the impact of ν for ϵ-values close to 1, which becomes less relevant, while for small or even negative ϵ-values it is important. In the case of $\epsilon = 0.1$, the $D = 5$ and $D = 7.5$ curves show similar critical current, because for $D = 5$ we are close to the optimal ν of 20%, while for $D = 7.5$, the curvature is close to optimal, which results (coincidentally) is the same critical current (J_c). However, for $D = 7.5$, $\nu > 40\%$, such that the voltage increases much more quickly above J_c. For larger ϵ, ν becomes less important which is seen for intermediate ϵ values, where $J_c(D = 7.5)$ is larger than $J_c(D = 5.0)$ despite the larger-than-optimal ν. For ϵ close to 1, also the curvature

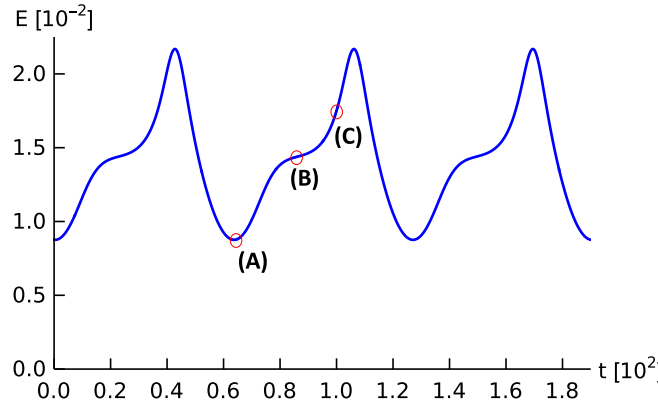

FIG. 3. Three periods of the time-dependent electric field $E(t)$ for $L = 10$, $\epsilon = 0.75$, and $D = 5$ with applied current $J_{dc} = 0.1$. Snapshots of the order parameter and vortex configurations at three distinct times (a)–(c) of a period are shown in Fig. 2.

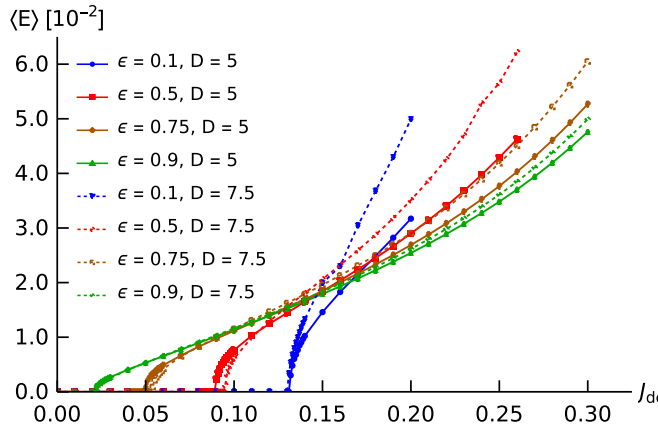

FIG. 4. J-E characteristics for five different sets of system parameters with $L = 10$ given in the legends. The electric field is averaged over $\gtrsim$10 periods of the vortex motion in the steady state for each current density and parameter set.

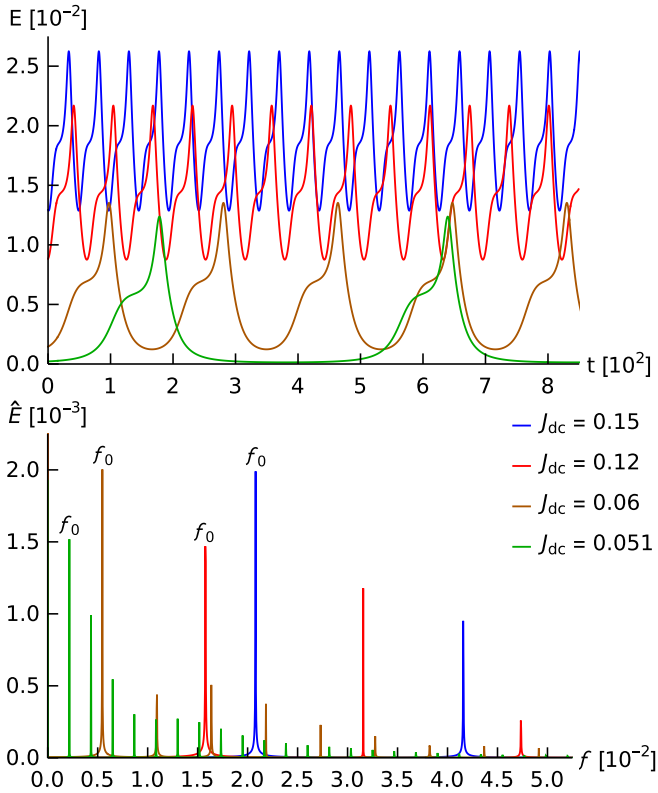

FIG. 5. (Top) Time-dependent electric field curves for the $L = 10$, $D = 5$, and $\epsilon = 0.75$ system with $J_{dc} = 0.051, 0.06, 0.12, 0.15$. (Bottom) The Fourier transforms of the $E(t)$ curves reveal the hopping frequencies $f_0 = 0.00217$, 0.00547, 0.01577, and 0.02080 for each of the applied currents respectively. The Fourier analysis also shows higher harmonics.

becomes less relevant and J_c is mostly determined by the difference $1 - \epsilon$.

Because the pinning sites are periodic, the resulting motion and associated electric field $E(t)$ will then show a regular oscillatory behavior with some current density-dependent hopping (or nucleation) frequency $f_0(J_{dc})$. Figure 3 shows the accompanying time-dependence of the electric field $E(t)$ across the system, where three distinct dynamical states are marked as (a)–(c), visualized in Fig. 2.

Figure 5(top) shows the behavior of $E(t)$ over a more extended time interval for different applied DC current densities, while Fig. 5(bottom) shows the corresponding Fourier transforms. Note that higher harmonics, $f_n \equiv nf_0$, are clearly visible. This is to be expected since the motion is highly inhomogeneous in both space and time.

It is clear that when J_{dc} increases, f_0 also increases, since higher current density can depin and translate the vortices faster, which increases the hopping frequency.

If we plot the hopping frequency as a function of applied DC current for various pinning site parameters, shown in Fig. 6, we notice almost the same functional dependence as the J-E characteristics (Fig. 4): In the critical region for J_{dc} near J_c we find a nonlinear dependence, $f_0 \propto J_{dc}^{\nu}$, where $\nu < 1$, after which it becomes approximately linear for higher applied current densities, as shown Fig. 6. However, as in

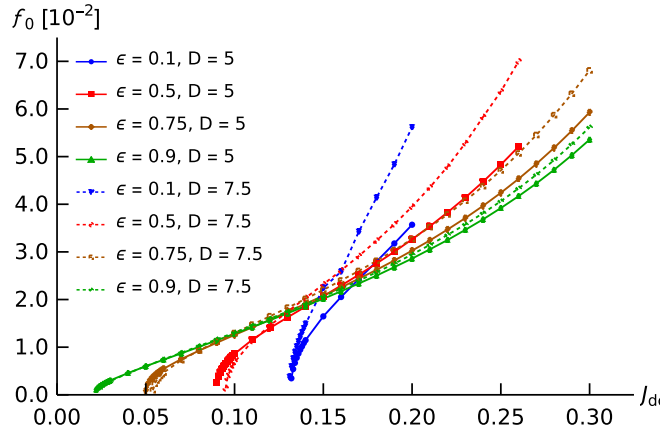

FIG. 6. Hopping frequencies as a function of applied DC current density, $f_0(J_{dc})$, for various system parameters with $L = 10$. The underlying oscillations of the electric field are caused by repeated periodic pinning and depinning events. The response frequencies are obtained by using the dominant peak of the Fourier transform of the electric field (calculated for $\gtrsim$65 periods of the vortex motion in the steady state), see Fig. 5.

the J-E characteristics, $f_0(J_{dc})$ becomes linear at very large current densities due to fluctuations of the order parameter amplitude.

Indeed, if we combine those two results and plot the average voltage, $\langle V \rangle = \sqrt{2}L\langle E \rangle$, as function of the hopping frequency f_0 all graphs (almost) perfectly collapse on a universal line with slope 4π, see Fig. 7, i.e., $\langle V \rangle = 2 \cdot 2\pi f_0$. This behavior is expected on the basis of Faraday's law in which two fluxons pin and depin at the same time within the unit cell in each period of f_0^{-1}:

$$V = nc^{-1}\phi_0 f. \tag{5}$$

In our dimensionless units, $c^{-1}\phi_0 = 2\pi$; n is the number of vortices in the simulated system, which is 2 for the unit cell. Alternatively, we identify the frequency occurring in Eq. (5) as the Josephson frequency $f_J = \frac{2e}{h}V$. This result is consistent with the analysis of Martinoli *et al.* [17] and Van Look *et al.* [18] of periodic line and hole arrays. Similar oscillatory

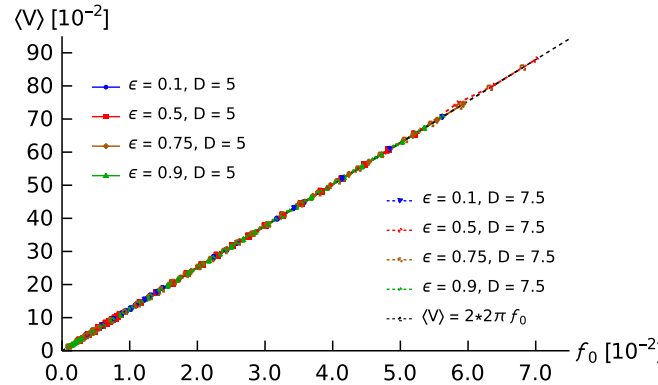

FIG. 7. The averaged voltage, $\langle V \rangle = \sqrt{2}L\langle E \rangle$, for eight different sets of system parameters with $L = 10$ given in the legends, the slope of the line is $2 \cdot 2\pi$. The electric field is averaged over $\gtrsim$10 periods of the vortex motion in the steady state for each current density and parameter set.

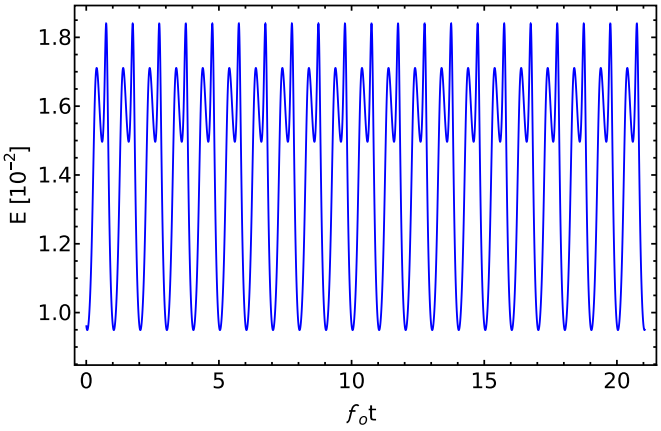

FIG. 8. Frequency locking for $f_{\rm ext} = f_0$ for the system of $J_{\rm dc} = 0.12$, $L = 10$, $D = 5$, and $\epsilon = 0.75$; the applied amplitude is $J_{\rm ac} = 0.02$. The plot shows a single-mode oscillation.

behavior has been seen in simulations of Josephson junction arrays [19,20].

IV. LOCKING TO AN EXTERNAL AC SOURCE

Next, we examine the effect of an additional AC component to the applied current density, $J_{\rm ac}\sin(2\pi f_{\rm ext}t)$, on the system. We find that $f_{\rm ext}$ and f_0 will synchronize for some range of applied frequencies in the vicinity of f_0 for a given $J_{\rm ac}$, where, depending on conditions, frequency locking appears, as shown in Fig. 8. By comparing Fig. 8 with Fig. 5, we see that oscillations have become more sinusoidal due to the influence of the applied frequency, $f_{\rm ext}$.

Figure 9 shows the result of applying a frequency outside, but close to, the range of frequencies where locking occurs. Note the oscillations acquire a low-frequency modulation seen as an envelope to the hopping frequency. These reflect the number of cycles over which the system locks, unlocks, and then relocks.

Figure 10 shows the locking regions for three different $J_{\rm ac}$ values.

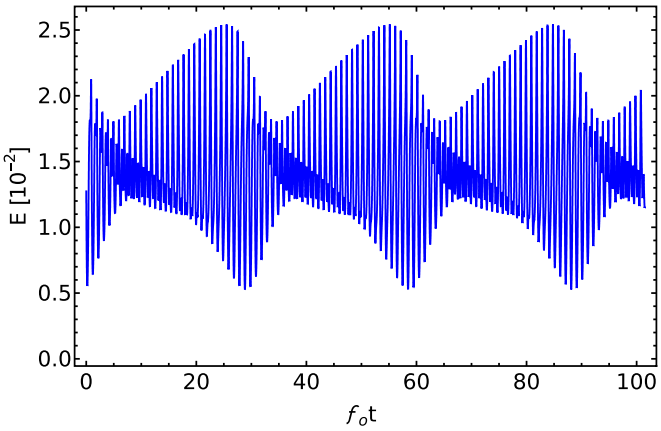

FIG. 9. Time-dependent electric field behavior of a $L = 10$, $D = 5$, and $\epsilon = 0.75$ system with applied $J_{\rm dc} = 0.12$, $J_{\rm ac} = 0.02$, and $f_{ext} = 1.046 f_0$. the envelope function is $f_{\rm env} = 5.632 \times 10^{-4}$, i.e., about 28 times lower than f_0.

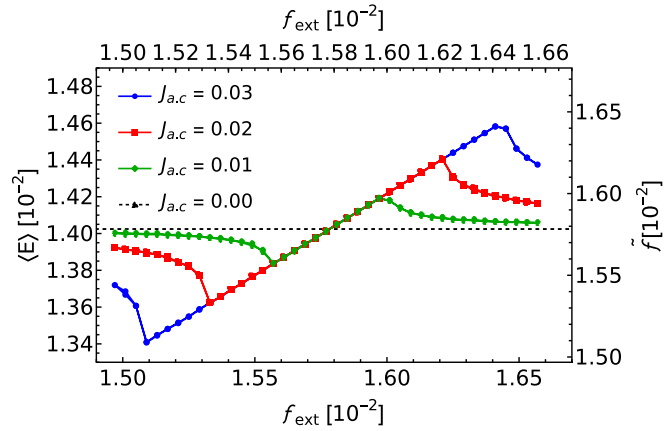

FIG. 10. Frequency locking region of the benchmark system with $L = 10$, $D = 5$, and $\epsilon = 0.75$ for different $J_{\rm ac}$ and fixed $J_{\rm dc} = 0.12$. Here, the electric field is averaged over $\sim 10^3$ periods of the vortex motion in the steady state.

Note that the locking region increases with increasing $J_{\rm ac}$. This behavior is due to the fact that f_0, strictly speaking, depends on $J_{\rm ext}$, which means that by adding the AC component, $f_0(J_{\rm ext})$ oscillates as well over an interval determined by $J_{\rm ac}$. The locking behavior can qualitatively be understood by comparison to the overdamped motion of a particle in a periodic potential under the influence of a DC plus AC driving force. This basically corresponds to the Langevin dynamics of a particle in a washboard potential, which is commonly used to describe the dynamics of a pancake vortex in 2D in a periodic pinning landscape. Since the dynamics in the locking regime is synchronized, the systems behavior can be compared to that of a single particle. Here the DC part of the current can be interpreted as the tilt of the periodic (pinning) potential resulting in the washboard potential. This simple equation of motion with external AC force results in a similar behavior of the particle velocity as the electric field dependence in the TDGL simulations, where the width of the locking region is indeed proportional to the AC amplitude.

Using Josephson's relation, $\langle E\rangle$ is converted to $\tilde{f}$, which we denote as the *response hopping frequency* appearing in the Fourier spectrum as the second highest peak, after the external frequency $f_{\rm ext}$. Both merge when the vortex dynamics in the system and the driving frequency are locked.

We can locate the locking region using three methods. First, we can observe the splitting of the fundamental peak in the Fourier spectrum, since when the system is synchronized with the applied AC current density, as shown in Fig. 8, the Fourier spectrum will show only a single peak at the applied frequency together with its harmonics. When the system is not locked the applied frequency will split off.

Secondly, one can measure the average DC electric field across the sample, which in turn is related to the response hopping frequency. This is done in Fig. 10. In general, this method is experimentally easier to measure than the time resolved field.

Finally, we can examine whether locking is present by analyzing the low-frequency modulation of the time-resolved electric field: If the system is locked, the envelope will have

constant amplitude (cf. Fig. 8); if not, we can determine the period of the envelope (see Fig. 9) and calculate the difference frequency.

Experimentally this frequency might be determined by rectifying the AC frequency and directly measuring the frequency of the modulation envelope.

We note that the locking phenomena simulated here are analogues to Shapiro steps observed in Josephson junctions when an external oscillator is applied with a frequency that has an integer relation to the Josephson frequency as verified by the experiments of Martinoli *et al.* [17] and Van Look *et al.* [18]; the configuration used by the latter group has been modeled by Reichhardt *et al.* [21].

V. GLOBAL STABILITY IN LARGER SYSTEMS

Quite generally the voltage drop across a current driven strip containing an array of vortices moving in some pinning landscape will consist of a superposition of contributions produced by their individually pinning and depinning from successive sites. In a spatially periodic lattice of pinning sites of the kind considered here there is the potential for a collective motion wherein all vortices hop synchronously from site to site. However, this is not necessarily the case and various instabilities can develop in which such a synchronous motion is lacking or breaks down; i.e., the hopping occurs at different times in different unit cells (see supplemental movie 2 [16]). In the simulations discussed in Sec. II B, the periodic boundary conditions utilized in our code were imposed on the unit cell of our pinning landscape, thereby forcing vortices in all unit cells in the periodically continued system to hop at the same time. To test for stability more generally, we enlarged the size of the simulated system to form a *super cell* that includes successively larger numbers of unit cells: $2 \times 2, 3 \times 3, 4 \times 4, \ldots$ The number of unit cells which fit horizontally, i.e., in the direction of the applied current, into the super cell is denoted as N_{sc}. The simulated super cells then consist of $N_{sc} \times N_{sc}$ unit cells. Again the unit cell used so far, is shown in Fig. 1.

As before, the applied magnetic field is the matching field corresponding to $2N_{sc}^2$ vortices. After relaxing the system from a random initial configuration in the super cell, we obtain a static state with one vortex pinned to each defect to which we then start to apply an external current. On increasing the applied current, one again reaches a critical value where, at least initially, the vortices de-pin and move as parallel columns perpendicular to the current. Note that the vortices within each column always move synchronously for our weak pinning sites and currents below the amplitude fluctuation regime. Here we refer to synchronous motion in a super cell as the simultaneous motion of adjacent vortex columns, which means all vortices in the super cell move at the same time, alternately pinning and depinning in unison. This synchronous motion typically breaks down when the current is increased to some threshold current, J_{th}, when some adjacent vortex columns loose their synchronization. Here, we calculate the value of J_{th} by starting with J_{dc} in the asynchronous regime and decreasing it to the point where synchronized hopping is recovered. Its dependence on the super cell size N_{sc} is shown in Fig. 11. As seen in the plot, it decreases as the size of system increases for smaller super cells. However, it is saturating in the asymptotic limit, implying an infinite system would be stable. Stability can be tested by either increasing or decreasing J_{dc} (in time) relative to J_{th} and examining the structure of the evolution of the array in time. Note that the J_{th} values plotted here also depend on the holding time at a fixed current during which the vortex matter reorganizes and eventually synchronizes and therefore represent a lower limit for its true adiabatic value (see supplemental movie 3 [16]). Therefore the apparent monotonic behavior seen in Fig. 11 is a result of the procedure we use to obtain this lower limit for J_{th}. In particular the nature of the asynchronous steady state we start from when lowering the current (in combination with the current step size) will result in variations of the time needed to establish synchronous motion once we reach currents $J_{dc} \leqslant J_{th}$. Furthermore, the synchronization time could exponentially depend on the super cell size as the rearrangement of vortices due to inter-vortex interactions follows glassylike dynamics. These timescales are not feasible to reach in a simulation (realistically we can simulate times up to 10's of microseconds). In any case we want to emphasize that once we observe synchronization at a particular current J_{dc}, the true threshold current is strictly bounded from below by that value. However, we expect that the threshold currents for adiabatically increasing and decreasing applied DC currents will coincide and thus not show any hysteresis.

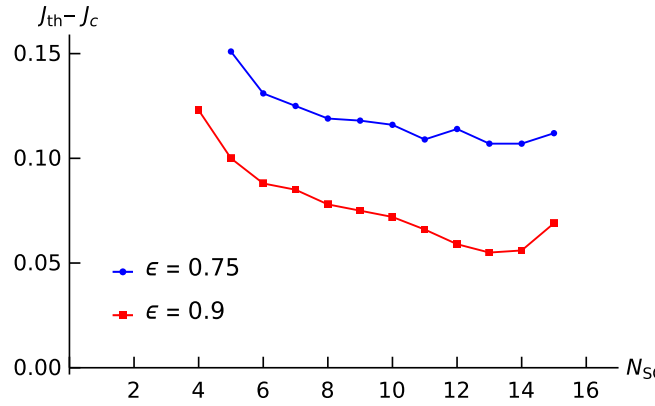

FIG. 11. The current difference, $J_{th} - J_c$, for the onset of asynchronous hopping with increasing super cell size, N_{sc} for two systems of $L = 10$ and $D = 5$ using different defect strength. The value of the critical currents $J_c = 0.05$ for the blue line, and $J_c = 0.022$.

When J_{dc} exceeds J_{th}, asynchronous hopping emerges. However, by applying an AC current with frequency comparable to the natural frequency for the applied DC current, synchronized hopping is recovered (see supplemental movie 4 [16]). This behavior can potentially be used as a low-temperature signal amplifier: by applying a small AC current to sample, it will generate a larger signal proportional to the applied J_{ac}.

The synchronization of the vortex motion is a result of the competing forces acting on the vortices. Most important are (i) the attractive one-body vortex-pinning site interaction, (ii) the (repulsive) two-body vortex-vortex interaction, and (iii) the Lorentz force resulting from the applied current. At high temperatures, thermal fluctuations can also affect the

TABLE I. Parameters for niobium (Nb) [26–28], molybdenum germanium (MoGe) [29,30], and $YBa_2Cu_3O_{7-x}$ (YBCO) at $x = 0.7$ (optimal) for c and ab planes [31,32].

quantity	Nb	MoGe	$YBCO_c$	$YBCO_{a,b}$
ξ_0	38nm	5nm	0.4nm	2nm
λ_0	39nm	500nm	800nm	150nm
σ	6.6×10^6 S/m	5.8×10^5 S/m	$\sim 10^6$ S/m	$\sim 10^6$ S/m
t_0	1.26×10^{-14} s	1.83×10^{-13} s	8.03×10^{-13} s	2.82×10^{-14} s
J_0	4.53×10^{12} A/m^2	2.10×10^{11} A/m^2	1.02×10^{12} A/m^2	5.82×10^{12} A/m^2

synchronization of vortices. In a homogeneous system without applied current, the inter-vortex force leads to the formation of the (hexagonal) Abrikosov vortex lattice. Since we are considering a dynamic situation here, the interplay of all these forces leads to the complex dynamic behavior we observe as compared to a static pinned lattice.

In particular, for large applied currents, the effect of pinning is "averaged out" and the system is governed mostly by the inter-vortex force. If this happens, the natural tendency for the vortex array is to adopt the Abrikosov lattice structure, as this is energetically the favored symmetry for a homogeneous film, thereby resulting in a dynamic phase transition between a square (imposed by the pinning sites) and a hexagonal vortex lattice above some average drift velocity (and associated current density). At that point, the oscillatory response with a single frequency is lost, as the vortex lattice is not commensurate with the pinning lattice anymore. In the pinning lattice nearest neighbor columns have a distance of $L/\sqrt{2}$, while a Abrikosov lattice with the same density has a vortex column distance of $L/\sqrt{2\sqrt{3}}$. Overall, this leads to a response frequency which is a multiple of the unit cell hopping frequency. At even higher currents beyond the dynamic phase transition, vortices start to move horizontally as well to switch between the natural distance and the imposed pinning site distance, which ultimately leads to completely incoherent vortex dynamics.

Our system has some similarity to the motion of a system of coupled oscillators such as in the Kuramoto model [22,23], but differs in that the one body pinning force is of finite range and hence bounded.

VI. MATERIAL PARAMETERS

To estimate the typical range of frequencies in actual materials, one needs to calculate the time scales involved using typical material parameters. For some superconductors of interest such as YBCO, niobium, and molybdenum germanium alloys (see Table I), we find that that $t_0 \sim 10^{-13}$s and $J_0 \sim 10^{12}$ A/m^2. Using the parameters of MoGe, one finds that for an applied current density $J_{dc} = 0.12$, the frequencies generated are of order, $f \sim 86$ GHz, with corresponding velocities $\langle v \rangle \sim 6$ km/s. Note that in practice we expect the velocities to be limited by the velocity of sound, which is exceeded at such velocities. Such current densities are rather high and possibly difficult to obtain experimentally. 86 GHz is a large frequency that has not been achieved in previous studies. Some reported frequencies are $f = 40$ MHz [18], $f \sim 500$ KHz–100 MHz [17], $f = 100$ MHz–1.5 GHz [24]. A recent study by Dobrovolskiy *et al.* [25] achieved vortices with a velocity of 10km/s, suggesting it may be possible to achieve higher frequencies. Note that near the critical current density ($J_{dc} = 0.051$), $f \sim 12$ GHz, and $\langle v \rangle \sim 0.8$ Km/s, which may be more easily achieved.

In realistic samples, we should also consider the effect of (bulk) disorder and edges on the dynamic behavior. To this end, we added a polycrystalline pattern with spatially randomized critical temperatures being close to the bulk T_c such that the artificial pinning sites are still much stronger than the disorder. The observed behavior is preserved with slightly reduced threshold current. To estimate the influence of edges, we replaced the periodic boundary condition in y direction (perpendicular to the vortex motion) by no-current conditions (see Ref. [12]) for larger supercells. The resulting edges cause random vortex nucleation at the entrance edge, which disrupts the synchronized motion near the critical current. This effect becomes smaller as we increase the applied current as long as it remains below the threshold current. However, if we remove the option for random vortex nucleation by introducing a row of notches matching the pinning site columns, the synchronization persists. Finally, we note that the estimated vortex velocities will heat the sample. However, we assume that any heat generated by the vortex motion can be effectively removed from the system. Experimentally, one can consider that the system is either immersed in a cryogenic liquid or that the substrate of the superconducting film is thermally anchored.

VII. CONCLUSION

Using the time dependent Ginzburg-Landau formalism, we have shown that above some critical current, J_c, a commensurate vortex lattice moving in a periodic pinning landscape of circular holes can generate an oscillating electric field at a certain inter pinning-site vortex hopping frequency. The hopping frequency, f_0, itself depends, not only on the system characteristics (lattice constant, hole size, and hole pinning strength), but also on the applied current. Adding an AC component to the applied DC current allows us to lock the hopping frequency to a range of applied frequencies which is near f_0. The range of the locking frequency interval depends also on the amplitude of the AC current.

In our initial simulations, we considered a square unit cell having a single vortex with a current applied perpendicular to an edge. However, in going over to larger systems comprised of multiple unit cells, called supercells, the synchronization of the vortex motion between neighboring unit cells was quickly lost. We then examined a 45° rotated square lattice with two vortices in an enlarged unit cell, with the current still per-

pendicular to an edge. When considering a supercell in this system the synchronization of the vortex motion was found to be stable below some threshold current density J_{th} that depends on the supercell size; furthermore, J_{th} approaches a limiting value with the increasing supercell size, implying an extended system can be stable below this value.

Since the applied current density can be varied, the systems studied here constitute miniature, current-tunable, oscillators that operate at cryogenic temperatures. They can be patterned directly into a strip-line wave guides with their output transmitted to other remote devices. The loss of synchronization observed at higher currents in larger systems can likely be minimized by patterning strips of finite width containing a limited number of columns.

The frequency can be modulated simply by varying the DC current density, J_{dc}, in time. Given that the vortex drift velocity responds quickly to a change in the applied current (since no narrow-band circuit elements are involved) these devices should switch on and off, or between differing frequencies, in times comparable to an oscillation period. The range of frequencies generated depends on the system parameters (hole geometry and separation) together with the superconducting materials of which it is made.

As seen from Fig. 5, the harmonic content of the signals produced can be quite high. For applications where this is undesirable it can be suppressed by engineering a smoother potential landscape; alternatively, one might want to exploit this feature.

Finally, there appears to be considerable potential that phenomena of the kind considered can lead to new devices based on the dynamics of vortex arrays moving in engineered artificial defect landscapes.

ACKNOWLEDGMENTS

This research was supported by the National Science Foundation under Grant No. 1905742, the U.S. Department of Energy, Office of Science, Basic Energy Sciences, Materials Sciences and Engineering Division, and finally through the computational resources and staff contributions provided for the Quest high performance computing facility at Northwestern University which is jointly supported by the Office of the Provost, the Office for Research, and Northwestern University Information Technology. Finally, we would like to thank Ivan Nevirkovets for some useful discussions concerning various experimental implications of the simulations described.

[1] A. T. Fiory, A. F. Hebard, and S. Somekh, Critical currents associated with the interaction of commensurate fluxline sublattices in a perforated Al film, Appl. Phys. Lett. **32**, 73 (1978).

[2] S. Raedts, A. V. Silhanek, M. J. Van Bael, and V. V. Moshchalkov, Flux-pinning properties of superconducting films with arrays of blind holes, Phys. Rev. B **70**, 024509 (2004).

[3] A. Hoffmann, P. Prieto, and I. K. Schuller, Periodic vortex pinning with magnetic and nonmagnetic dots: The influence of size, Phys. Rev. B **61**, 6958 (2000).

[4] J. I. Martín, M. Vélez, J. Nogués, and I. K. Schuller, Flux Pinning in a Superconductor by an Array of Submicrometer Magnetic Dots, Phys. Rev. Lett. **79**, 1929 (1997).

[5] D. J. Morgan and J. B. Ketterson, Asymmetric Flux Pinning in a Regular Array of Magnetic Dipoles, Phys. Rev. Lett. **80**, 3614 (1998).

[6] I. A. Sadovskyy, A. E. Koshelev, A. Glatz, V. Ortalan, M. W. Rupich, and M. Leroux, Simulation of the vortex dynamics in a real pinning landscape of $YBa_2Cu_3O_{7-\delta}$ coated conductors, Phys. Rev. Appl. **5**, 014011 (2016).

[7] I. A. Sadovskyy, Y. Jia, M. Leroux, J. Kwon, H. Hu, L. Fang, C. Chaparro, S. Zhu, U. Welp, J.-M. Zuo, Y. Zhang, R. Nakasaki, V. Selvamanickam, G. W. Crabtree, A. E. Koshelev, A. Glatz, and W.-K. Kwok, Toward superconducting critical current by design, Adv. Mater. **28**, 4593 (2016).

[8] A. E. Koshelev, I. A. Sadovskyy, C. L. Phillips, and A. Glatz, Optimization of vortex pinning by nanoparticles using simulations of the time-dependent Ginzburg-Landau model, Phys. Rev. B **93**, 060508(R) (2016).

[9] G. Kimmel, I. A. Sadovskyy, and A. Glatz, In silico optimization of critical currents in superconductors, Phys. Rev. E **96**, 013318 (2017).

[10] G. J. Kimmel, A. Glatz, V. M. Vinokur, and I. A. Sadovskyy, Edge effect pinning in mesoscopic superconducting strips with non-uniform distribution of defects, Sci. Rep. **9**, 211 (2019).

[11] I. A. Sadovskyy, A. E. Koshelev, W.-K. Kwok, U. Welp, and A. Glatz, Targeted evolution of pinning landscapes for large superconducting critical currents, Proc. Natl. Acad. Sci. USA **116**, 10291 (2019).

[12] I. Sadovskyy, A. Koshelev, C. Phillips, D. Karpeyev, and A. Glatz, Stable large-scale solver for Ginzburg Landau equations for superconductors, J. Comput. Phys. **294**, 639 (2015).

[13] W.-K. Kwok, U. Welp, A. Glatz, A. E. Koshelev, K. J. Kihlstrom, and G. W. Crabtree, Vortices in high-performance high-temperature superconductors, Rep. Prog. Phys. **79**, 116501 (2016).

[14] N. Kopnin, *Theory of Nonequilibrium Superconductivity*, International Series of Monographs on Physics (Oxford University Press, 2001)

[15] I. A. Sadovskyy, Y. L. Wang, Z.-L. Xiao, W.-K. Kwok, and A. Glatz, Effect of hexagonal patterned arrays and defect geometry on the critical current of superconducting films, Phys. Rev. B **95**, 075303 (2017).

[16] See Supplemental Material at http://link.aps.org/supplemental/10.1103/PhysRevB.xx.xxxxxx for movies of the time evolution of superconducting order parameter.

[17] P. Martinoli, O. Daldini, C. Leemann, and E. Stocker, A.c. quantum interference in superconducting films with periodically modulated thickness, Solid State Commun. **17**, 205 (1975).

[18] L. Van Look, E. Rosseel, M. J. Van Bael, K. Temst, V. V. Moshchalkov, and Y. Bruynseraede, Shapiro steps in a superconducting film with an antidot lattice, Phys. Rev. B **60**, R6998 (1999).

[19] G. R. Berdiyorov, S. E. Savelev, F. V. Kusmartsev, and F. M. Peeters, In-phase motion of josephson vortices in stacked SNS

Josephson junctions: effect of ordered pinning, Supercond. Sci. Technol. **26**, 125010 (2013).

[20] G. R. Berdiyorov, S. Savel'ev, F. V. Kusmartsev, and F. M. Peeters, Effect of ordered array of magnetic dots on the dynamics of josephson vortices in stacked SNS Josephson junctions under dc and ac current, Eur. Phys. J. B **88**, 286 (2015).

[21] C. Reichhardt, R. T. Scalettar, G. T. Zimányi, and N. Grønbech-Jensen, Phase-locking of vortex lattices interacting with periodic pinning, Phys. Rev. B **61**, R11914 (2000).

[22] Y. Kuramoto, International symposium on mathematical problems in theoretical physics, Lect. Notes Phys. **30**, 420 (1975).

[23] S. H. Strogatz and R. E. Mirollo, Collective synchronisation in lattices of nonlinear oscillators with randomness, J. Phys. A: Math. Gen. **21**, L699 (1988).

[24] O. V. Dobrovolskiy, R. Sachser, M. Huth, V. A. Shklovskij, R. V. Vovk, V. M. Bevz, and M. I. Tsindlekht, Radiofrequency generation by coherently moving fluxons, Appl. Phys. Lett. **112**, 152601 (2018).

[25] O. V. Dobrovolskiy, D. Y. Vodolazov, F. Porrati, R. Sachser, V. M. Bevz, M. Y. Mikhailov, A. V. Chumak, and M. Huth, Ultra-fast vortex motion in a direct-write Nb-C superconductor, Nat. Commun. **11**, 3291 (2020).

[26] J. Eisenstein, Superconducting elements, Rev. Mod. Phys. **26**, 277 (1954).

[27] C. Kittel, *Introduction to Solid State Physics*, 8th ed. (Wiley, 2004).

[28] A. Leo, G. Grimaldi, R. Citro, A. Nigro, S. Pace, and R. P. Huebener, Quasiparticle scattering time in niobium superconducting films, Phys. Rev. B **84**, 014536 (2011).

[29] A. Y. Rusanov, M. B. S. Hesselberth, and J. Aarts, Depairing currents in superconducting films of Nb and amorphous MoGe, Phys. Rev. B **70**, 024510 (2004).

[30] J. Draskovic, T. R. Lemberger, B. Peters, F. Yang, J. Ku, A. Bezryadin, and S. Wang, Measuring the superconducting coherence length in thin films using a two-coil experiment, Phys. Rev. B **88**, 134516 (2013).

[31] U. Welp, W. K. Kwok, G. W. Crabtree, K. G. Vandervoort, and J. Z. Liu, Magnetic Measurements of the Upper Critical Field of $YBa_2Cu_3O_{7-\delta}$ Single Crystals, Phys. Rev. Lett. **62**, 1908 (1989).

[32] M. Chiao, R. W. Hill, C. Lupien, L. Taillefer, P. Lambert, R. Gagnon, and P. Fournier, Low-energy quasiparticles in cuprate superconductors: A quantitative analysis, Phys. Rev. B **62**, 3554 (2000).